Coherently confined single-metal-atom chains in 2D semiconductors

Wen Qin [1,8], Shasha Guo [2,8], Zixi Liu[1,3], Peikun Zhang[1], Chao Zhu[4], Yao Wu [5], Ruixi Qiao [1,3] ✉, Zheng Liu [6,7] ✉, Wanlin Guo [1] ✉ & Zhuhua Zhang [1] ✉

Single-metal-atom chains (SMACs) possess a variety of unique properties and functionalities but suffer from ambient vulnerability due to their delicate one-atom-width structures. While some SMACs can be effectively stabilized by nanochannel confining, it remains a pressing challenge to experimentally realize more versatile atomic chains with sufficient stability and extended length. Here, we propose a computational protocol to identify transition metals capable of forming SMACs along mirror twin boundaries in two-dimensional metal dichalcogenides. Taking MoS_2 as a prototypical example, our thermodynamics and kinetics calculations indicate that Co, Ni, Rh, Pd, and Pt atoms can be enticed by the progressive formation of mirror twin boundaries to yield robust SMACs; whereas other transition metal elements tend to result in either substitutional doping or nanoclusters. These findings are supported by successful experimental synthesis of Co-, Ni-, Pd- and Pt-based SMACs using a chemical vapor co-deposition method, which exhibit high stability due to their covalent bonding with MoS_2 grains. These results lay a solid foundation for investigating exotic transport behaviors within extremely confined channels.

Dimensionality is a key factor determining the properties and functionalities of nanomaterials, since it dictates how electrons interact and behave by altering the symmetry and potential fields in materials. For instance, zero-dimensional (0D) nanoclusters exhibit quantized energy levels, while two-dimensional (2D) materials provide delocalized states of electrons confined in a planar space. Among them, one-dimensional (1D) nanostructures have attracted special research interest[1,2], since they represent the smallest dimension that maintains efficient electron transports, and, thus, have been deemed critical to the functionality and integration of nanoscale devices[3]. Single-metal-atom chains (SMACs)—the ultimate manifestations of 1D structures—can confine electrons within an absolutely 1D space. This characteristic renders SMACs as a unique platform to investigate a series of intriguing quantum transport behaviors and correlation effects[4,5], including quantized conductance[6,7], magnetoresistance[8], Peierls transition[9] and Tomonaga–Luttinger liquid[10–12], opening up a wealth of opportunities for cutting-edge applications in electronics[13], magnetism[14], and optics[15].

There have been two typical synthesis approaches for fabricating SMACs, one is the top-down mechanical stretching method for suspended SMACs, and the other is the self-assembly method for supported SMACs. However, the atomic chains fabricated using these

[1]State Key Laboratory of Mechanics and Control for Aerospace Structures, Key Laboratory for Intelligent Nano Materials and Devices of Ministry of Education, and Institute for Frontier Science, Nanjing University of Aeronautics and Astronautics, Nanjing 210016, China. [2]Department of Chemistry and Chemical Biology, Cornell University, Ithaca, NY 14853, USA. [3]Center for Microscopy and Analysis, Nanjing University of Aeronautics and Astronautics, Nanjing 210016, China. [4]SEU-FEI Nano-Pico Center, Key Lab of MEMS of Ministry of Education, School of Electronic Science and Engineering, Southeast University, Nanjing 210096, China. [5]Department of Materials Science and Engineering, National University of Singapore, 9 Engineering, Drive 1, Singapore 117575, Singapore. [6]School of Materials Science and Engineering, Nanyang Technological University, Singapore 639798, Singapore. [7]CINTRA CNRS/NTU/THALES, UMI 3288, Research Techno Plaza, Singapore 639798, Singapore. [8]These authors contributed equally: Wen Qin, Shasha Guo. ✉e-mail: rxqiao@nuaa.edu.cn; z.liu@ntu.edu.sg; wlguo@nuaa.edu.cn; chuwazhang@nuaa.edu.cn

methods suffer from low yield and limited chain length, largely due to sophisticated experimental procedures[16,17]. Moreover, most of the reported SMACs exhibit structural vulnerability and poor ambient stability since all their atoms are highly undercoordinated[18]. Recently, we have pioneered a chemical vapor co-deposition (CVCD) method enabling the fabrication of Pt SMACs network at wafer scale. The as-fabricated Pt SMACs exhibit structural stability up to 1000 K and an average length of up to tens of nanometers. Aside from the Pt SMACs, the CVCD growth method is, in principle, applicable to a range of transition metals (TMs) for synthesizing similar SMACs. However, experimental synthesis of SMACs out of numerous choices of elements in a trial-and-error manner is expensive and inefficient. Therefore, there is an urgent need to develop a predictive theory for guiding the experimental synthesis based on a deep understanding of the formation mechanism.

Herein, we propose a theoretical protocol for computationally screening TM atoms that can form stable atomic chains by exploiting mirror twin boundaries in hexagonal metal dichalcogenides MX_2 (M = Mo, W; X = S, Se, Te). The key factors for screening the TMs include the possibility of substitution doping, surface clustering, edge adsorption, and the kinetic growth of TM-decorated edges. Taking MoS_2 as an example, we identify 5 elements—Co, Ni, Rh, Pd, and Pt—from a list of 27 TM elements, which can theoretically form air-stable SMACs. Among them, Co, Ni, Pd, and Pt chains are confirmed by our CVCD experiments (confirmation for Rh is infeasible due to precursor limitation). These results reveal a general growth process for 1D confined atomic chains and can be extended to synthesize a range of peculiar nanostructures by exploring various confinements intrinsic to 2D materials.

Results and discussion
Four-step screening protocol
Our previous work has shown that the key factor in the synthesis of Pt SMACs lies in the behavior of Pt precursor, which is supplied in the form of pre-deposited uniform nanoclusters, with sizes and average spacings of only a few nanometers. In a typical CVCD experiment, these TM nanoclusters serve two important functions: (i) inducing massive nucleation of MX_2 nanograins, and (ii) facilitating the incorporation of TM single atoms into the MX_2 lattice[19]. These nanoclusters exhibit notable size-dependent melting behavior[20] (Supplementary Fig. 1), leading to a liquid phase under typical growth temperature, which promotes atom diffusion and the formation of thermodynamically stable structures. However, to form highly ordered SMACs, single TM atoms need to be precisely delivered to the grain boundaries in a thermodynamically and kinetically favorable manner (Fig. 1a). This behavior strongly depends on the intrinsic properties of the element itself. For example, when diffusing on the MoS_2 surface, TM atoms with high chemical activity tend to be trapped by the host lattice in the form of substitutional doping, while those with high cohesive energies tend to form metal aggregations. In both cases, the early depletion of available TM atoms hinders their migration to the growth front of MoS_2. Moreover, even if TM atoms reach the MoS_2 domain edge and are adsorbed there, this edge decoration may suppress the kinetic growth of MoS_2 domain—another obstacle for the SMAC formation. The stable edge adsorption configurations of TM atoms are also required to satisfy the stoichiometric requirement of forming a complete SMAC when two growing grains are stitched along the grain boundary.

To this end, guided by key processes of SMAC growth kinetics, we designed a four-step screening protocol—i.e., calculations of substitution doping, surface clustering, and edge adsorption of TM atoms, as well as kinetic growth barrier of TM-decorated edges—termed SSEK (Fig. 1b). We adopted MoS_2 as the prototypical MX_2 host. Throughout the screening procedures, 27 TM elements of the periods 4–6 in the periodic table were systematically assessed, which we will discuss step by step in the following sections.

Substitution doping in MoS₂ grains
Thermodynamically favorable substitutional doping of TM atoms into the MoS_2 host lattice hampers SMAC formation at grain boundaries. Thus, we first examine its possibility by calculating the dominating factor, substitution energy (E_s) for a TM atom to replace a native atom, given by the following equation:

$$E_s = E_{tot} - E_{MoS_2} + \mu_{native} - \mu_{TM} \tag{1}$$

where E_{MoS_2} and E_{tot} denote the total energies of the MoS_2 lattice before and after TM doping, and μ_{native} and μ_{TM} are the chemical potentials of the replaced native atom (i.e., Mo or S) and the doped TM atom, respectively[21]. Here, μ_{TM} is taken as the energy of a single TM atom in the bulk phase, while the value of μ_{native} (i.e., μ_{Mo} or μ_S) depends on the given growth condition.

At thermodynamic equilibrium, the chemical potentials of Mo (μ_{Mo}) and S (μ_S) satisfy following equation:

$$\mu_{MoS_2} = \mu_{Mo} + 2\mu_S \tag{2}$$

where μ_{MoS_2} is the total energy of a MoS_2 unit cell. Given the S-rich condition in our CVCD process, we assumed that the chemical potential of S atom in the growth system is equivalent to that of element sulfur (S_2 molecular), that is, $\mu_S^{S-rich} = \mu_S^0$. Subsequently, we have the chemical potential of Mo atom following equation:

$$\mu_{Mo}^{S-rich} = \mu_{MoS_2} - 2\mu_S^0 \tag{3}$$

We employed a 5×5 monolayer MoS_2 supercell for including one doped TM atom to minimize the effect of interactions between TM atoms in adjacent images (Supplementary Fig. 2). Note that TM substitution at the S sites is excluded, given the positive E_s for all TM atoms (Supplementary Table 1). Therefore, TM substitution at the Mo sites was carefully studied. As shown in Fig. 2a, E_s strongly depends on TM, ranging from -4.05 to 3.70 eV. The trend of E_s values increasing from left to right within the same period suggests a reduced likelihood of substitution as the atomic number increases. To assess the thermodynamic feasibility of TM substitution, we employed an exothermic reaction ($E_s<0$) as our selection criterion. Applying this rule, we excluded 15 TM elements (Sc, Ti, V, Cr, Mn, Fe, Y, Zr, Nb, Ru, Hf, Ta, W, Re, and Os) located in the blue region of Fig. 2a. A part of these elements with a propensity of substitutional doping in 2D MX_2, such as Ti, V, Cr, Mn, Fe, Nb, W, and Re, have been validated in previous experiments[22–26].

Atoms clustering on the MoS₂ surface
Prior to the CVCD process, nanosized (0.5–2 nm) TM clusters were pre-deposited to initiate MoS_2 nucleation and subsequently form SMACs[19]. At the growth temperature (650 °C), increased thermal fluctuations tend to disrupt the unstable "amorphous" state of TM precursor, leading to the formation of more stable configurations. TM atoms experience two primary interactions on the MoS_2 surface: a vertical interaction with the MoS_2 substrate (TM-MoS_2) and a lateral interaction with adjacent TM atoms (TM-TM). The competition between these two interactions largely influences SMAC formation. A stronger TM-MoS_2 interaction tends to attract TM atoms from the nanocluster to the MoS_2 surface, positively charging them and resulting in monodispersed TM atoms, known as the monodispersed phase[27]. In contrast, a weaker TM-MoS_2 interaction favors the formation of an initial TM aggregated phase, progressing into large clusters (Supplementary Fig. 3).

To thermodynamically quantify the structural evolution of TM atoms on MoS_2 surface, binding energy (negative), cohesive energy (negative), and diffusion barrier (positive) are introduced. The binding energy ($E_b = E_{TM-MoS_2} - E_{MoS_2} - \mu_{TM}$) quantifies the interaction
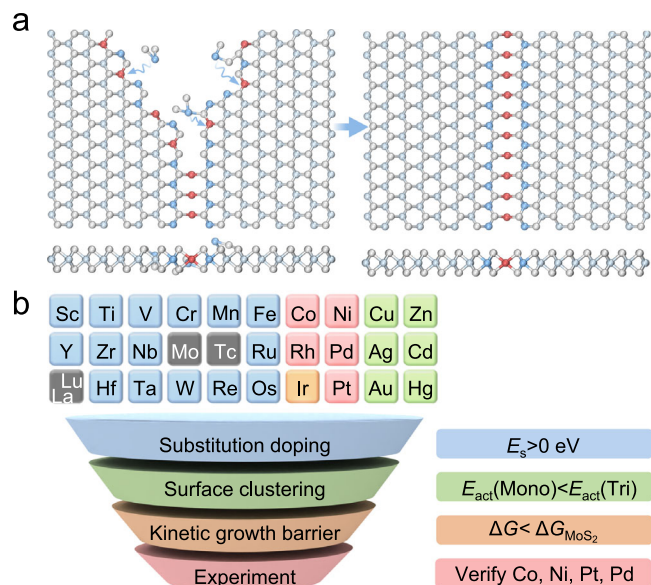
Fig. 1 | SMACs growth and screen process. a The formation of SMACs. Two antisymmetric MoS_2 grains with appropriately adsorbed TM atoms at edges are stitching together during kinetic edge growth, resulting in the formation of SMACs at mirror twin boundary. The light blue and silver spheres represent the Mo and S atoms, respectively. The red spheres represent the TM atoms adsorbed on the edges, while the blue spheres denote the newly incorporated Mo atoms during growth. b Flowchart for screening TM elements capable of forming SMACs. 27 TM elements are evaluated through substitution doping (blue), surface clustering (green), kinetic growth barrier (orange), and experimental verification (red). Corresponding criteria and experimental result are listed on the right. The elements excluded by each criterion are marked with corresponding colors. The successful synthesis of Co, Ni, Pt and Pd SMACs was verified through our CVCD growth.

Fig. 2 | Screening of TM atoms through substitution doping and surface clustering. a Histogram diagram of substitution energy (E_s) of TM atoms at the Mo site under S-rich condition. The TM atoms with negative E_s in the blue region tend to dope into the MoS_2 lattice, while those with positive E_s in the red region are unfavorable to substitute. b Activation energy (E_{act}) as a function of TM atom binding energy (E_b) to pristine MoS_2 monolayer, rendering a volcanic curve. The left-hand and right-hand sides of the curve favor the monomer and trimer phases for the adsorbed TM atoms, respectively. Inset presents the free energy evolution of initially monodispersed Ag atoms on the MoS_2 surface during AIMD simulation, with snapshots showing a transition to the cluster structure.

strength between an individual TM atom and the basal plane of MoS_2 surface. The cohesive energy ($E_c = (E_{TM} - n \times \mu_{TM})/n$) quantifies the cohesion strength between TM atoms adsorbed on the MoS_2 surface. The surface diffusion barrier (E_{db}) quantifies the ability of TM atoms to diffuse on the MoS_2 surface[28]. Generally, a strong binding to the MoS_2 surface and a weak cohesive strength with the neighboring TM atoms will favor the dispersed monomers on MoS_2. Conversely, a weak binding to MoS_2, a strong cohesion between TM atoms, and a high diffusion barrier of TM on MoS_2 will favor the formation of TM clusters. Following the analysis in Ref. 27., we define the activation energy for the monodispersed phase of TM atoms by following equation:
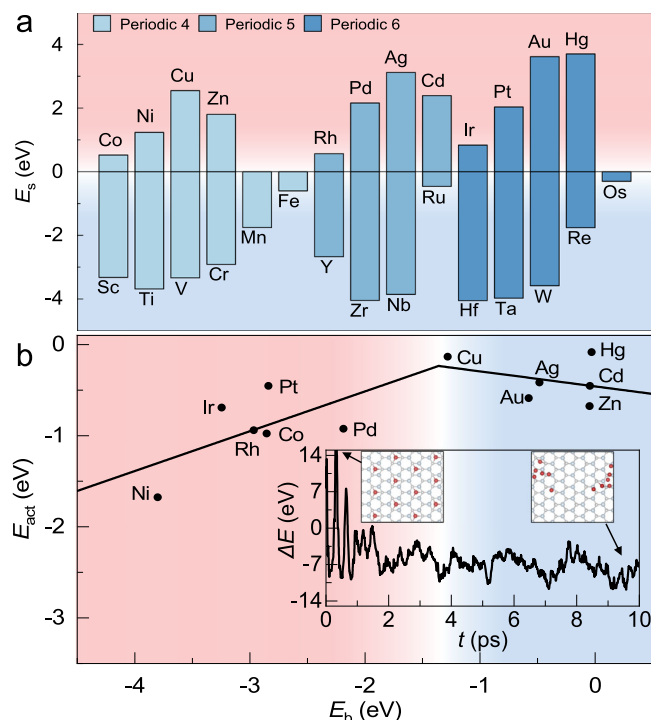
$$E_{act}(MO) = E_b - E_c \quad (4)$$

and define the activation energy for the cluster phase of TM atoms (exemplified by trimer) on MoS_2 by following equation:

$$E_{act}(TRI) = -E_b + E_c - E_{db} \quad (5)$$

Here the trimer phase is chosen to represent the initial state of the aggregated phase since the trimerization of TMs on the transition dichalcogenides has been predicted to be stable on MX_2 surfaces[29] and been confirmed in several experiments[30,31].

Extensive calculations and analysis revealed a linear-like scaling relationship between E_c and E_b, fitted as $E_c = 0.51E_b - 0.53 (R^2 = 0.85)$. Similar relationship also exists between E_{db} and E_b, reading as $E_{db} = -0.27E_b + 0.02 (R^2 = 0.9)$ (Supplementary Fig. 4). These results could be rationalized by that a stronger binding of a TM atom to the substrate corresponds to its more difficult diffusion and potentially a higher cohesive energy with other TM atoms. Therefore, the activation energies can be simplified as: $E_{act}(MO) = 0.49E_b + 0.53$

and $E_{act}(TRI) = -0.22E_b - 0.55$. As shown in Fig. 2b, the activation energy follows a volcano-like trend with respect to E_b, peaking at -1.37 eV/atom. For elements positioned on the left side, the TM-MoS_2 interaction dominates, resulting in a lower $E_{act}(MO)$ value to favor a thermodynamically preferred monodispersing phase. In contrast, for elements falling on the right side, a lower $E_{act}(TRI)$ value makes the trimer phase more favorable. By comparing the values of $E_{act}(MO)$ and $E_{act}(TRI)$, we proceeded to screen the remaining 12 TM candidates, identifying Ni, Ir, Rh, Pt, Co, and Pd as the elements tending to be monodispersed on MoS_2 for further evaluation. In addition, this volcano-like principle is further corroborated by ab initio molecular dynamics simulations. Taking Ag as an example, our simulations indicate that the initially monodispersed Ag atoms tend to aggregate following a 10-ps relaxation at 923 K (Fig. 2b, inset). This result aligns well with experimental observations of Ag nanoparticles on the MoS_2 surface, instead of monodispersed atoms[32].

Adsorption structures at MoS_2 edges

The monodispersed TM atoms will diffuse on the MoS_2 surface under thermal fluctuation and preferentially dock at the edges, where the TM atoms are tightly bound to form stable configurations. Thus, we investigated the adsorption structures of TM atoms at MoS_2 edges, marking the initial stage of SMAC growth.

To search for the ground state structure, various configurations are tested by considering different edge structures, adsorption sites, and coordination numbers (Fig. 3a and Supplementary Table 2). It is noteworthy that S-terminated zigzag edges were chosen to align with the S-rich condition[33]. First, we studied the adsorption on an ideal
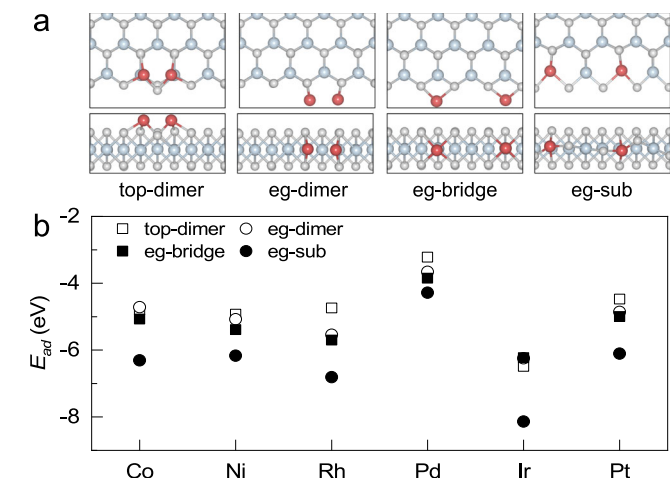
Fig. 3 | Adsorption energy of TM atoms on MoS₂ edges. a Structures of the top-dimer, eg-dimer, eg-bridge, and eg-sub configurations. **b** Adsorption energy (E_{ad}) of TM atoms with different edge adsorption configurations as listed in (**a**). The light blue, silver, and red spheres represent the Mo, S, and TM atoms, respectively.

S-terminated zigzag edge. The interaction between the adsorbed TM atoms and the MoS₂ edges[34] are quantified by the adsorption energy, expressed by following equation:

$$E_{ads} = (E_{tot} - E_{MoS_2} - n \times \mu_{TM})/n \qquad (6)$$

where n is the number of adsorbed TM atoms around the edge. Among the enumerated configurations, three—named as top-dimer, eg-dimer, and eg-bridge—are validated to be relatively stable due to their lower adsorption energies (Fig. 3a). In these names, "top" and "eg" signify whether the TM atoms are adsorbed on top or on the side of the edge Mo atoms; "dimer" indicates two TM atoms are adsorbed adjacently to form a dimer; and "bridge" signifies a TM atom spanning over two adjacent S sites. As shown in Fig. 3b, eg-bridge configuration exhibits the lowest E_{ads} for Co, Ni, Rh, Pd, and Pt. Conversely, Ir shows the lowest E_{ads} with the top-dimer configuration (Supplementary Fig. 5).

During the kinetic growth process, the real MoS₂ edge structure deviates from the ideal scenario due to non-uniform addition of Mo and S atoms, potentially impacting the most stable TM adsorption configuration. Therefore, second, we conducted growth kinetics analysis initialized with eg-bridge and top-dimer configurations for the respective TM elements. Our results show a notable reduction in the total energy of the system upon the addition of Mo and S atoms, suggesting the presence of a lower energy edge adsorption configuration, denoted as eg-sub (Fig. 3a). This configuration exhibits a reconstructed MoS₂ edge with single S atoms terminating the metal atoms, resembling TM atoms substituting every alternate edge Mo. Further calculations demonstrate that E_{ads} of the eg-sub configuration lies at the energy minima for all the six TM elements (Fig. 3b). Thus, such a configuration is adopted as the grain edge for the following SMAC growth.

Growth kinetics of SMAC

Similar to the traditional CVD growth processes of MX₂ and h-BN characterized by edge nuclei and subsequent advancement of the edges[35,36], the growth of SMACs should also start from the TM-decorated MoS₂ edges and maintained by the accretion of feeding stocks thereat. This implies that newly added Mo and S atoms during kinetic growth should intercalate between current MoS₂ edge and adsorbed TM atoms until the merging of MoS₂ grains and the formation of grain boundaries.
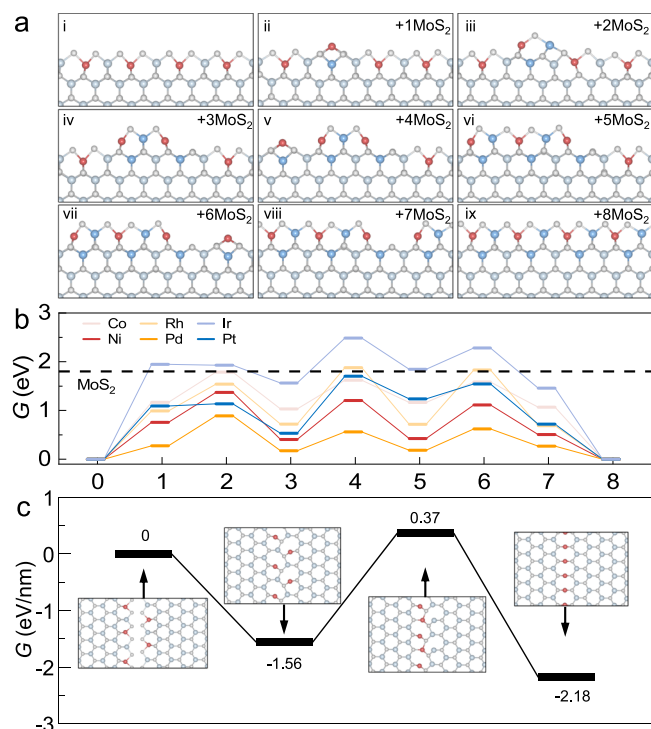
Fig. 4 | Growth kinetics at TM-decorated edges. a Energetically optimal atomic configurations during the step-by-step addition of Mo+2S units to the Ni eg-sub zigzag edge. The light blue and silver spheres represent the Mo and S atoms, respectively. The red spheres represent the Ni atoms adsorbed on the edges, while the blue spheres denote the newly incorporated Mo atoms during growth. **b** The optimal energy pathways for the kinetic growth along the edges decorated with different TM atoms. The black dashed line indicates the energy barrier for the kinetic growth at a pristine MoS₂ edge. We set $\Delta\mu_{MoS_2} = 0$ eV, representing the equilibrium condition. **c** Schematic formation of the Ni SMAC, along with the evolution of total energy during the formation of SMAC via atomic reorganization near the grain boundary. As two oppositely oriented grains are about to coalesce, Ni atoms at two opposite eg-sub edges can migrate toward each other to self-assemble into the SMAC by an exothermic process.

Based on the edge energy calculations set forth above, we calculate the growth kinetics for MoS₂ with the most favorable eg-sub edge configuration (Fig. 4a and Supplementary Fig. 6). Under practical growth condition, the precursors MoO₃ and S₂ form derivatives, such as MoS₆[37], which then dock at the MoS₂ edge to maintain the growth at a stoichiometric ratio of S/Mo of 2. To simplify the computational process, Mo+2S units are added step-by-step to the eg-sub edge for simulating the near-equilibrium growth. Furthermore, we choose the configurations with the lowest energy at each step as the base structures for the subsequent atomic accretion. This approach, dubbed nanoreactor model, enables us to draw the optimal energy pathway and extract the energy barrier of growth kinetics, and has been successfully applied to understand the kinetic growth mechanisms of graphene[38], boron nitride[35] and borophene[39].

Taking the growth process of Ni-decorated edges as an example, when a Mo+2S unit is introduced initially, a Ni atom is displaced to the MoS₂ growth front, adopting a 4-ring eg-bridge structure (Fig. 4a, i-ii). Following the addition of the second Mo+2S unit, the previous 4-ring structure transforms into a tilted hexagonal ring structure with sites available for further growth (Fig. 4a, iii). Upon the introduction of the third Mo+2S unit, the second Ni atom is extracted to the growth front, leading to the formation of the second hexagonal ring structure. At this stage, an edge segment resembling the eg-sub configuration starts to be formed, thus exhibits relatively low system energy (Fig. 4a, iv). Notably, the addition of 4th Mo+2S unit energetically prefers
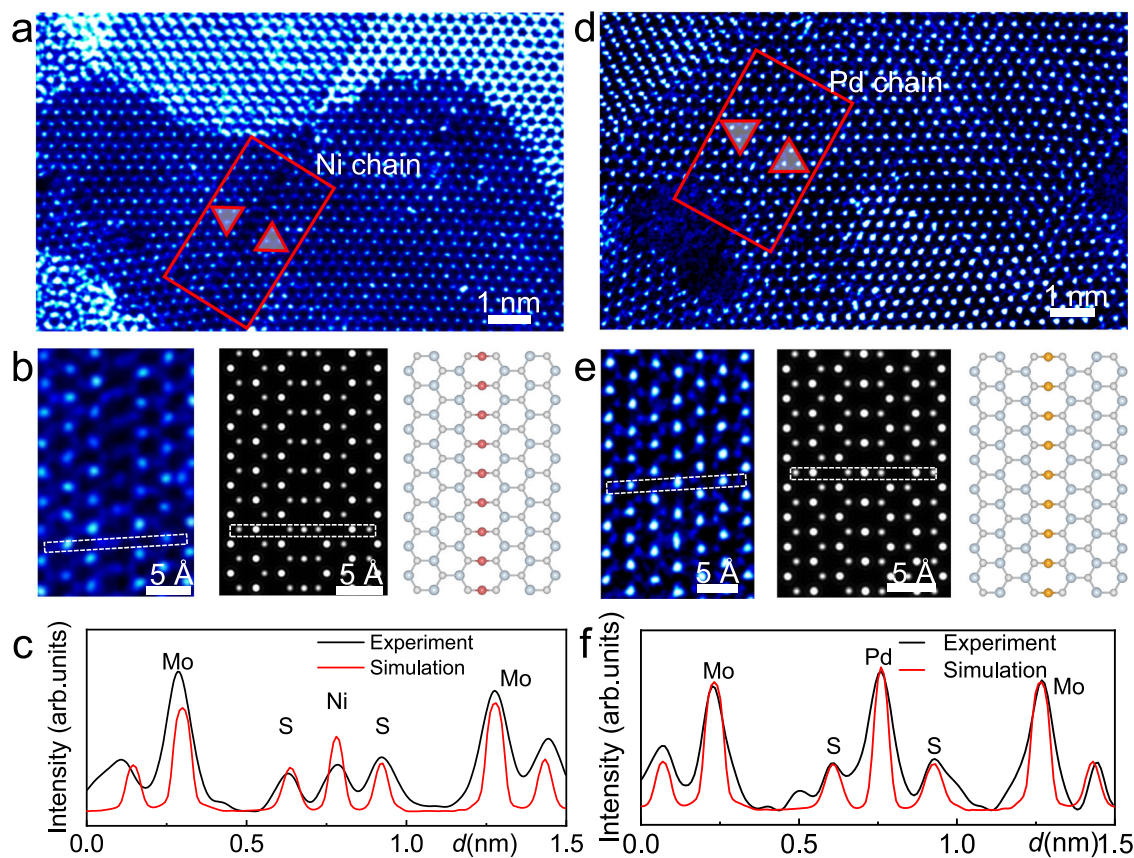
Fig. 5 | STEM characterizations of Ni and Pd SMACs in MoS₂. a, d False-colored HAADF-STEM images of Ni (**a**) and Pd (**d**) SMACs in MoS₂. **b, e** Magnified, simulated HAADF-STEM images and atomic models of Ni (**b**) and Pd (**e**) SMACs corresponding to the red rectangular area marked in (**a**) and (**d**), respectively. **c, f** Intensity profiles of the experimental and simulated images of Ni (**c**) and Pd (**f**) SMACs along the white dashed boxes in (**b**) and (**e**).

extracting the third Ni atom embedded at the original MoS₂ edge, rather than directly extending the hexagonal rings further (Fig. 4a, v and Supplementary Fig. 7). The addition of the 5th Mo+2S unit draws the newly extracted Ni atoms to the hexagonal ring structure (Fig. 4a, vi), extending the newly formed eg-sub segment. Notably, the energy in the step (vi) closely mirrors that of the step (iv), with only a 0.02 eV difference. Further addition of Mo+2S units alternately repeats steps (v) and (vi), driving the seamless extension of the MoS₂ lattice while preserving the eg-sub edge configuration.

The free energy profiles for the various TM atom-decorated edges along the optimal growth pathway are illustrated in Fig. 4b. It turns out that the edge growth of MoS₂ involving Ni, Co, and Pd decorations follows a similar progression, with the second step acting as the rate-determining one. The corresponding energy barriers are recorded at 1.37, 1.79, and 0.87 eV, respectively, lower than the growth barrier of 1.80 eV for the pristine MoS₂ edge. In contrast, the fourth step defines the energy barrier for the edge growth involving Ir, Pt and Rh atoms, showing a value of 2.48, 1.7, and 1.88 eV, respectively.

Next, we examine the growth rate of eg-sub edge decorated with TM atoms. Artyukhov et al. derived that the growth rate of an atomically flat edge is proportional to $e^{-(\Delta G_N^* + \Delta G_P^*)/2k_BT}$, where ΔG_N^* and ΔG_P^* represent the critical nucleation free energy barrier and the propagation free energy barrier for the edge growth, respectively[38], k_B is the Boltzmann constant and T the temperature. Since the introduction of TM precursors has been demonstrated to facilitate the nucleation of grains and the formation of SMACs are mainly determined by the extension and the final coalescence of grains, we assume that the growth rate relevant to our purpose is dominated by the kinetic barrier of edge growth, i.e., ΔG_P^*. Our results indicate that the Ir-decorated edge (with the highest ΔG_P^* of 2.48 eV) exhibits a growth rate four

orders of magnitude lower than that of the Pd-decorated edge (with the lowest ΔG_P^* of 0.87 eV) and even two orders of magnitude lower than that of the pristine MoS₂ edge (with ΔG_P^* of 1.8 eV) at the experimental temperature of 923 K. The significantly lower growth rate of Ir-decorated grains than bare grains not only reduces the chance of SMAC formation but also results in structural disorder in nucleated SMACs, since the pristine edges with no metal decoration can dominate the overall growth in this case.

As shown in Fig. 4c, when two oppositely oriented MoS₂ grains with the preserved eg-sub edge grow and merge, mirror twin boundary appears in-between, and the Ni atoms self-assemble within the 1D channel. After a certain period of thermal fluctuation, the Ni atoms at two opposite edges move toward each other and are re-organized to form SMAC embedded in the mirror twin boundary. This entire process releases 2.18 eV/nm of energy by overcoming an energy barrier of only 0.37 eV/nm. Note that mirror twin boundaries exclusively support the formation of continuous SMACs, whereas other boundary types yield fragmented segments or disordered doping (Supplementary Fig. 8). Furthermore, we conducted AIMD simulations to examine the structure stability of the as-formed five SMACs. The results indicate that all the five SMACs exhibit excellent structure stability, potentially withstanding temperatures as high as 1000 K (Supplementary Fig. 9).

Experimental confirmation of SMAC synthesis
Our SSEK protocol has theoretically identified five TM candidates (Co, Ni, Rh, Pd, and Pt) for constructing SMAC in MoS₂ hosts. Among these elements, wafer-scale production of Pt SMAC has been successfully demonstrated in our prior research[19], whereas the confirmation of Rh SMAC is currently difficult due to our experimental restriction (specifically, the unavailability of high-quality deposition of Rh
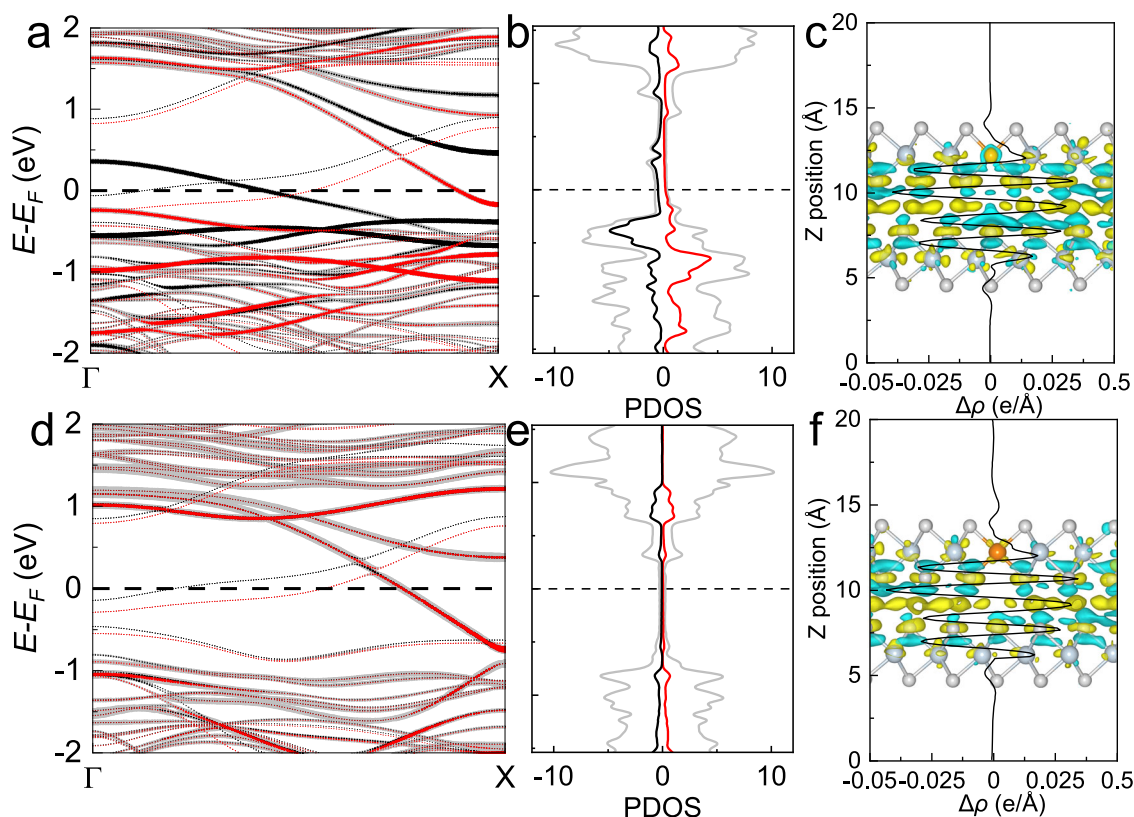
Fig. 6 | Electronic properties and charge densities of Co and Pd SMACs.
a, d Electronic band structures of the Co (**a**) and Pd (**d**) SMACs embedded in MoS_2. The band structures are projected onto SMACs and surrounding atoms. The grey lines represent the total contribution from the TM atoms and the adjacent MoS_2 hexagonal ring (unshaded regions marked in Supplementary Fig. 15a). Red lines represent the contribution of spin-up states from TM atoms and adjacent bonded S atoms (red box marked in Supplementary Fig. 15a), while the black lines represent contribution of spin-down states. The weight character of bands is thickness encoded. **b, e** Spin-polarized DOS of the Co (**b**) and Pd (**e**) SMACs embedded in MoS_2. The grey lines represent the total DOS from the unshaded regions marked in Supplementary Fig. 15a. The red lines represent DOS of spin-up states from Co and Pd d orbits, while black lines represent DOS of spin-down states. The Fermi levels (E_F) are set as 0 eV and highlighted by the black dashed line. **c, f** The planar-averaged charge density difference profiles between pristine and Co (**c**) or Pd (**f**) SMAC-containing MoS_2 monolayers along the z-direction. Insets show isosurface plots (0.00015 $e/Å^3$) of the corresponding real-space charge density distributions. The charge accumulation and depletion regions are colored yellow and blue, respectively.

nanoclusters). Therefore, we conducted CVCD experiments with carefully optimized growth conditions (see Methods) focusing on Co, Ni, and Pd to validate our theoretical predictions.

High-angle annular dark-field scanning transmission electron microscopy (HAADF-STEM) was employed to characterize the detailed atomic structures of synthesized samples. In virtue of the Z-contrast nature ($\sim Z^{1.5}$) of HAADF, elements with different atomic numbers (Z) can be explicitly distinguished. The results unequivocally demonstrated the successful synthesis of Ni, Pd, and Co SMACs within the mirror twin boundaries of MoS_2 grains, where hexagonal honeycomb lattice indicates the formation of MoS_2 nanocrystals and a distinct contrast change was observed in the boundary region of two oppositely oriented MoS_2 grains (highlighted by red triangles) (Fig. 5a, d, and Supplementary Fig. 10a). Unlike Pt SMAC, Co and Ni atoms exhibited lower contrast in MoS_2 lattice due to their smaller atomic numbers, while the Pd atom presented a slightly larger contrast than Mo (Pd and Mo have similar atomic numbers), which agrees well with the simulated results (Fig. 5b, c, e, f and Supplementary Fig. 10b, c). Zoom-in images surrounding MoS_2 boundaries (marked by red boxes) were investigated to resolve the atomic structures of SMACs. It confirms that atomically straight 1D TM channels were formed in MoS_2 boundaries, where the TM atoms bonded to S-zigzag edges on both sides and were confined in the Mo atomic plane of MoS_2 host (Fig. 5b, e and Supplementary Fig. 10b). This result contrasts the conventional MoS_2 mirror twin boundary structures without TM incorporated, which are composed of 4-fold rings with S_2-site point sharing (4 | 4 P)

or edge sharing (4 | 4E)[40,41]. The line profile analysis along Ni, Pd and Co SMACs indicated similar atomic spacings (3.17, 3.18, and 3.18 Å, respectively); all the values are significantly larger than their bulk case but close to the MoS_2 lattice constant, suggesting a tunable lattice constant of SMACs by varying host materials. Additionally, large-area HAADF-STEM characterizations reveal consistent ratios for Pt, Co, Ni, and Pd SMAC in mirror twin boundaries of polycrystalline MoS_2 films, and confirm SMAC formation in MoS_2 multilayers (Supplementary Figs. 11 and 12). Notably, the MoS_2 monolayer on different substrates differ in the formed SMACs. The MoS_2 on a SiO_2/Si substrate exhibits extensive formation of Pt chains, along with a small amount of dispersed Pt atoms, whereas that on a sapphire substrate displays more dispersed Pt atoms, in addition to the formation of Pt chains[19].

In addition to these successful examples, we also examined some elements that were predicted unfavorable for forming SMACs. For example, our experiments demonstrated substitutional doping of Nb and Fe atoms in the corresponding synthesized samples (Supplementary Fig. 13). Previous experiments also demonstrated clustering behaviors on MoS_2 surfaces when Au, Cu, or Ag precursors were introduced during the CVD growth[32,42–44]. All these results are well consistent with our theory, confirming the validity of the SSEK screening protocol we proposed. Furthermore, we expect that SMACs can form along the MTBs in other 2D MX_2 systems, notably in WS_2, as supported by the synthesis of Mo-based SMACs at the 2H/1 T phase interfaces in WS_2[45].

Metallic behavior of SMAC

To further explore the potential interactions within the Co, Ni, and Pd SMACs, an analysis was conducted on the characteristics of partial charge density distribution on the *d* orbitals of these elements. Supplementary Fig. 14 shows a noticeable non-localized electron density distribution between neighboring Co, Ni, and Pd atoms, underscoring the potential role of SMACs as electron transport channels. Additionally, band structures and projected density of states (DOS) were computed for the Co, Ni, and Pd SMACs. Compared to the band structure of pristine MoS_2 crystal, the introduction of SMACs in MoS_2 results in the emergence of electron bands near the Fermi level (as shown in Fig. 6a, d and Supplementary Fig. 15b). The *d* orbital electrons of Co, Ni, and Pd atoms fill the gap of the pristine MoS_2 near the Fermi level, thereby resulting in the metallic nature within a semiconducting matrix (as shown in Fig. 6b, e and Supplementary Fig. 15c). The metallic behavior benefits from the close enough distance between adjacent TM atoms in the SMACs (~3.2 Å), which enables a significant overlap of *d* electron states between the TM atoms.

Meanwhile, according to the orbital-projected DOS (Fig. 6b), splitting occurs between the spin-up and spin-down states of the Co 3*d* orbitals. As a result, the magnetic moment of Co-SMAC is mainly contributed by the Co 3*d* orbital with a value of 0.6 μ_B per atom, lower than the experimental value for bulk Co (~1.7 μ_B per atom)[46]. Conversely, Pd atoms within the corresponding SMAC show a non-magnetic behavior (Supplementary Fig. 16). Moreover, charge transfer analysis between two stacked MoS_2 layers indicated that sulfur atoms in the bottom MoS_2 layer donate electrons to confined Co and Pd atoms in the top MoS_2 layer (Fig. 6c, f), indicating an effective modulation of work function of the MoS_2 layer by SMACs (Supplementary Table 3).

We have developed a computational protocol to screen the TM atoms capable of forming SMACs coherently confined in 2D metal dichalcogenides. The protocol delves into four steps involving TM atoms substitution, surface clustering, edge adsorption, and kinetic edge growth, thus termed SSEK, all critical in the SMAC formation. Our SSEK method suggests that only Co, Ni, Pd, Pt, and Rh can form SMACs in 2D MoS_2, and the former four are confirmed in our experimental synthesis. The combined theory and experiments further establish the edge-dominated formation mechanism of SMACs. Moreover, metallic and even magnetic properties are predicted for these SMACs, which originate from substantial overlap of TM electronic states. These results open a promising pathway to efficiently fabricating SMACs in diverse 2D hosts and offer powerful 1D platforms for investigating quantum conduction, Tomonaga-Luttinger liquids, and other exotic physical phenomena in 1D scenarios.

Methods

CVCD growth of Pt/Co/Ni/Pd SMACs

First, the targeted transition metal nanoclusters were deposited on clean SiO_2/Si or sapphire wafers using electron-beam evaporation at a rate of 0.1 Å s^{-1} for 10 s. Second, the prepared metal-coated SiO_2/Si wafers and other precursors were loaded into the reaction chamber of a furnace. Specifically, the wafers were placed facing downward on an aluminum oxide boat containing MoO_3 powder in the center of a quartz tube, and sulfur powder was loaded in another crucible upstream in the tube. Third, after purging the CVD system by 500 standard cubic centimeters per minute (sccm) argon flow for 3 min, the center of the furnace was heated from room temperature to the growth temperature with a ramp of ~50 °C min^{-1} under continuous argon gas flows of 60 sccm. The SMACs within the MoS_2 films were synthesized by maintaining the reaction temperature at 650 °C for 4 min, while maintaining the sulfur source at around 230 °C. Finally, the furnace was naturally cooled down under the protective argon atmosphere.

DFT calculations

The substitution and surface clustering simulations were simulated with a $5 \times 5 \times 1$ supercell of a monolayer MoS_2. The monolayer was separated by a 15 Å vacuum space in *z* direction to isolate neighbor periodic images. A $2 \times 2 \times 1$ k-mesh was used to sample the first Brillouin zone of the model. The adsorption structure of TM atoms on MoS_2 S zigzag edge was simulated using a $4 \times 4 \times 1$ model, with *y* direction being continuous while *x* and *z* directions separated by 15 Å vacuum slabs. The adsorption model was sampled by a $1 \times 3 \times 1$ k-mesh. The eg-sub edge structure of growth simulation using a $4 \times 8 \times 1$ model, with *y* direction being continuous while *x* and *z* directions separated by 15 Å vacuum slabs. The model was sampled by a k-mesh with similar density. Spin-polarization was considered in all the calculations. The cut-off energy was set to be 500 eV. The convergence criteria were 10^{-5} eV for the self-consistent field energy and 0.01 eV/Å for the residual forces on each atom, respectively. The calculations were performed based on the projector-augmented wave method implemented in the Vienna ab initio simulation package (VASP) code[47–49]. The generalized gradient approximation (GGA) with Perdew-Burke-Ernzerhof (PBE) functional was employed to solve the Kohn-Sham density functional theory[50–52].

In ab-initio molecular dynamics simulations for SMACs in monolayer MoS_2, the edges are passivated with sulfur atoms. The Brillouin zone was sampled with a $(1 \times 20 \times 1)$ *k*-point mesh for geometry optimizations, and a $(1 \times 80 \times 1)$ mesh for electronic structure calculations. The electronic band calculations were performed by combining the VASP with post-processing VASPKIT package[53]. For electronic structure calculation, we performed an electronic self-consistent field procedure with tetrahedron method using Blöchl corrections. The thermal stability of TM atoms SMACs in MoS_2 structure was evaluated by an ab-initio molecular dynamic simulation using NVT ensemble. The simulation was run at 1000 K, and the time step was set to 1 fs.

The charge density difference map is generally plotted to view the redistribution of charges after the interaction. Through the calculation and analysis of different charge density, it is possible to obtain the properties of charge redistribution. The definition formula of differential charge density is:

$$\Delta\rho = \rho_{\text{bilayerMoS}_2} - \rho_{\text{TM-MoS}_2\text{layer}} - \rho_{\text{MoS}_2\text{layer}} \qquad (7)$$

where $\rho_{\text{bilayerMoS}_2}$ is the charge density of the entire system, $\rho_{\text{TM-MoS}_2\text{layer}}$ is the charge density of the TM- MoS_2 layer, and $\rho_{\text{MoS}_2\text{layer}}$ is the charge density of perfect MoS_2 layer.

STEM characterizations

The SMAC samples were first transferred onto commercial TEM grids through a standard wet transfer method and the STEM experiments were then performed in a Thermal Fisher Spectra 300 operated at 300 kV with a convergence semi-angle of about 24.5 mrad and collection semi-angle of 50–200 mrad. STEM image simulations were carried out with the Dr. Probe package[54], and the simulated parameters were set based on the experimental conditions.

Data availability

The source data underlying Figures are provided as a Source Data file. Source data are provided with this paper.

References

1. De Volder, M. F. et al. Carbon nanotubes: present and future commercial applications. *Science* **339**, 535–539 (2013).
2. Law, M. et al. Semiconductor nanowires and nanotubes. *Annu. Rev. Mater. Res.* **34**, 83–122 (2004).
3. Hu, J. et al. Chemistry and physics in one dimension: synthesis and properties of nanowires and nanotubes. *Acc. Chem. Res.* **32**, 435–445 (1999).

4.   Zhang, Z. et al. Size-dependent phononic thermal transport in low-dimensional nanomaterials. *Phys. Rep.* **860**, 1–26 (2020).

5.   Ozpineci, A. & Ciraci, S. Quantum effects of thermal conductance through atomic chains. *Phys. Rev. B* **63**, 125415 (2001).

6.   Requist, R. et al. Metallic, magnetic and molecular nanocontacts. *Nat. Nanotechnol.* **11**, 499–508 (2016).

7.   Zhang, J. et al. Peculiar atomic bond nature in platinum monatomic chains. *Nano Lett.* **21**, 3922–3928 (2021).

8.   Smogunov, A. et al. Colossal magnetic anisotropy of monatomic free and deposited platinum nanowires. *Nat. Nanotechnol.* **3**, 22–25 (2008).

9.   Blumenstein, C. et al. Symmetry-breaking phase transition without a peierls instability in conducting monoatomic chains. *Phys. Rev. Lett.* **107**, 165702 (2011).

10. Wang, P. et al. One-dimensional Luttinger liquids in a two-dimensional moiré lattice. *Nature* **605**, 57–62 (2022).

11. Zhang, H. et al. Tomonaga-luttinger liquid in the topological edge channel of multilayer FeSe. *Nano Lett.* **21**, 6253–6260 (2021).

12. Xia, Y. et al. Quantum confined tomonaga-luttinger liquid in Mo_6Se_6 nanowires converted from an epitaxial $MoSe_2$ monolayer. *Nano Lett.* **20**, 2094–2099 (2020).

13. Tang, C. S. et al. 1D chain structure in 1T'-phase 2D transition metal dichalcogenides and their anisotropic electronic structures. *Appl. Phys. Rev.* **8**, 1 (2021).

14. Shang, C. et al. Atomic wires of transition metal chalcogenides: a family of 1D materials for flexible electronics and spintronics. *JACS Au* **1**, 147–155 (2021).

15. Xia, Y. et al. One-dimensional nanostructures: synthesis, characterization, and applications. *Adv. Mater.* **15**, 353–389 (2003).

16. Fukuzumi, R. et al. Formation of a chain-like water single molecule junction with Pd electrodes. *J. Phys. Chem. C* **122**, 4698–4703 (2018).

17. Bera, J. K. & Dunbar, K. R. Chain compounds based on transition metal backbones: new life for an old topic. *Angew. Chem. Int. Ed.* **41**, 4453–4457 (2002).

18. Smit, R. H. M. et al. Common origin for surface reconstruction and the formation of chains of metal atoms. *Phys. Rev. Lett.* **87**, 266102 (2001).

19. Guo, S. et al. Direct growth of single-metal-atom chains. *Nat. Synth.* **1**, 245–253 (2022).

20. Nanda, K. et al. Liquid-drop model for the size-dependent melting of low-dimensional systems. *Phys. Rev. A* **66**, 013208 (2002).

21. Dolui, K. et al. Possible doping strategies for MoS_2 monolayers: Anab initiostudy. *Phys. Rev. B* **88**, 075420 (2013).

22. Li, M. et al. Vanadium doped 1T MoS_2 nanosheets for highly efficient electrocatalytic hydrogen evolution in both acidic and alkaline solutions. *Chem. Eng. J.* **409**, 128158 (2021).

23. Zhou, J. et al. A library of atomically thin metal chalcogenides. *Nature* **556**, 355–359 (2018).

24. Robertson, A. W. et al. Atomic structure and spectroscopy of single metal (Cr, V) substitutional dopants in monolayer MoS_2. *ACS Nano* **10**, 10227–10236 (2016).

25. Cai, Z. et al. Dual-additive assisted chemical vapor deposition for the growth of Mn-doped 2D MoS_2 with tunable electronic properties. *Small* **16**, e1903181 (2020).

26. Sovizi, S. & Szoszkiewicz, R. Single atom doping in 2D layered MoS_2 from a periodic table perspective. *Surf. Sci. Rep.* **77**, 100567 (2022).

27. Zhang, P. et al. Mechanism regulating self-intercalation in layered materials. *Nano Lett.* **23**, 3623–3629 (2023).

28. Sheppard, D. et al. A generalized solid-state nudged elastic band method. *J. Chem. Phys.* **136**, 074103 (2012).

29. Sun, Y. et al. Interface-mediated noble metal deposition on transition metal dichalcogenide nanostructures. *Nat. Chem.* **12**, 284–293 (2020).

30. Lin, Y. C. et al. Revealing the atomic defects of WS_2 governing its distinct optical emissions. *Adv. Funct. Mater.* **28**, 1704210 (2018).

31. Song, Z. et al. Line defects in monolayer $TiSe_2$ with adsorption of Pt atoms potentially enable excellent catalytic activity. *Nano Res.* **15**, 4687–4692 (2022).

32. Gong, C. et al. Metal contacts on physical vapor deposited monolayer MoS_2. *ACS Nano* **7**, 11350–11357 (2013).

33. Cheng, J. et al. Kinetic Nature of Grain Boundary Formation in As-Grown MoS_2 Monolayers. *Adv. Mater.* **27**, 4069–4074 (2015).

34. Umrigar, C. & Wilkins, J. W. Adsorption site, adsorption energy, and normal vibration frequency of H on Ni (100) via total-energy calculations. *Phys. Rev. Lett.* **54**, 1551 (1985).

35. Zhang, Z. et al. Growth mechanism and morphology of hexagonal boron nitride. *Nano Lett.* **16**, 1398–1403 (2016).

36. Dong, J. et al. Edge reconstruction-dependent growth kinetics of MoS_2. *ACS Nano* **17**, 127–136 (2023).

37. Lei, J. et al. Gas-phase "Prehistory" and molecular precursors in monolayer metal dichalcogenides synthesis: the case of MoS_2. *ACS Nano* **15**, 10525–10531 (2021).

38. Artyukhov, V. I. et al. Equilibrium at the edge and atomistic mechanisms of graphene growth. *Proc. Natl. Acad. Sci. USA* **109**, 15136–15140 (2012).

39. Zhang, Z. et al. Near-equilibrium growth from borophene edges on silver. *Sci. Adv.* **5**, eaax0246 (2019).

40. Van Der Zande, A. M. et al. Grains and grain boundaries in highly crystalline monolayer molybdenum disulphide. *Nat. Mater.* **12**, 554–561 (2013).

41. Zhou, W. et al. Intrinsic structural defects in monolayer molybdenum disulfide. *Nano Lett.* **13**, 2615–2622 (2013).

42. Li, M. et al. Thermostable 1T-MoS_2 nanosheets achieved by spontaneous intercalation of Cu single atoms at room temperature and their enhanced HER performance. *Small Struct.* **4**, 2300010 (2023).

43. He, Y. et al. Engineering grain boundaries at the 2D limit for the hydrogen evolution reaction. *Nat. Commun.* **11**, 57 (2020).

44. Jing, D. et al. Non-equilibrium growth of metal clusters on a layered material: Cu on MoS_2. *N. J. Phys.* **22**, 053033 (2020).

45. Wang, Z. et al. One-dimensional atomic segregation at semiconductor–metal interfaces of polymorphic transition metal dichalcogenide monolayers. *Nano Lett.* **18**, 6157–6163 (2018).

46. Gambardella, P. et al. Ferromagnetism in one-dimensional monatomic metal chains. *Nature* **416**, 301–304 (2002).

47. Kresse, G. & Joubert, D. From ultrasoft pseudopotentials to the projector augmented-wave method. *Phys. Rev. B* **59**, 1758 (1999).

48. Kresse, G. & Furthmuller, J. Efficient iterative schemes for ab initio total-energy calculations using a plane-wave basis set. *Phys. Rev. B: Condens. Matter* **54**, 11169–11186 (1996).

49. Blochl, P. E. Projector augmented-wave method. *Phys. Rev. B: Condens. Matter* **50**, 17953 (1994).

50. Perdew, J. P. et al. Atoms, molecules, solids, and surfaces: applications of the generalized gradient approximation for exchange and correlation. *Phys. Rev. B* **46**, 6671 (1992).

51. Perdew, J. P. & Wang, Y. Accurate and simple analytic representation of the electron-gas correlation energy. *Phys. Rev. B* **45**, 13244 (1992).

52. Perdew, J. P. et al. Generalized gradient approximation made simple. *Phys. Rev. Lett.* **77**, 3865 (1996).

53. Wang, V. et al. VASPKIT: a user-friendly interface facilitating high-throughput computing and analysis using VASP code. *Comput. Phys. Commun.* **267**, 108033 (2021).

54. Barthel, J. Dr. Probe: a software for high-resolution STEM image simulation. *Ultramicroscopy* **193**, 1–11 (2018).

Acknowledgements

Author contributions

Z.Z. conceived the idea. Z.Z. discussed with R.Q., Z.L., W.G. and designed the project. W.Q. and P.Z. conducted the DFT calculations. S.G. conducted the synthesis experiments. R.Q., C.Z., Y.W., Z.-X.L. and S.G. conducted the STEM characterizations of SMACs. W.Q. and S.G. wrote the manuscript with inputs form R.Q., Z.L., W.G., and Z.Z.

Competing interests

The authors declare no competing of interest.

Additional information

Supplementary information The online version contains supplementary material available at
https://doi.org/10.1038/s41467-025-60127-3.

Correspondence and requests for materials should be addressed to Ruixi Qiao, Zheng Liu, Wanlin Guo or Zhuhua Zhang.

Peer review information *Nature Communications* thanks Guangtong Liu, Jiong Zhao and the other, anonymous, reviewer(s) for their contribution to the peer review of this work. A peer review file is available.

Reprints and permissions information is available at
http://www.nature.com/reprints

Publisher's note Springer Nature remains neutral with regard to jurisdictional claims in published maps and institutional affiliations.